PHOTONICS Research

All-silicon dual-cavity fiber-optic pressure sensor with ultralow pressure-temperature cross-sensitivity and wide working temperature range

Xue Wang,[1,2] Junfeng Jiang,[1,3] (iD) Shuang Wang,[1,4] Kun Liu,[1] (iD) and Tiegen Liu[1,5]

[1]School of Precision Instrument and Opto-electronics Engineering, Tianjin Optical Fiber Sensing Engineering Center, Institute of Optical Fiber Sensing of Tianjin University, Key Laboratory of Opto-electronics Information Technology, Tianjin University, Tianjin 300072, China
[2]School of Electrical and Electronic Engineering, Engineering Research Center of Optoelectronic Devices and Communication Technology, Ministry of Education, Tianjin Key Laboratory of Film Electronic and Communication Devices, Tianjin University of Technology, Tianjin 300384, China
[3]e-mail: jiangjfjxu@tju.edu.cn
[4]e-mail: shuangwang@tju.edu.cn
[5]e-mail: tgliu@tju.edu.cn

Pressure-temperature cross-sensitivity and its accompanying temperature-related stability is a nerve-wracking obstruction for pressure sensor performance in a wide temperature range. To solve this problem, we propose a novel (to the best of our knowledge) all-silicon dual-cavity optical Fabry–Perot interferometer (FPI) pressure sensor. The all-silicon structure has high intrinsic reflectivity and is able to eliminate the influence of thermal-expansion-mismatch-induced stress and chemical-reaction-induced gas generation, and therefore, in essence, enhances measurement accuracy. From the experiment results, the pressure-temperature cross-sensitivity is reduced to be ~5.96 Pa/°C, which presents the lowest pressure-temperature cross-sensitivity among the FPI pressure sensors with the capability of surviving high temperatures up to 700°C thereby opening the way for high-precision pressure monitoring in various harsh and remote environments.   © 2021 Chinese Laser Press

https://doi.org/10.1364/PRJ.414121

1. INTRODUCTION

Pressure sensing can provide rich interaction force information related to the object and is of significant importance in artificial intelligence input devices [1], electronic skin [2,3], organ system medical pressure monitoring [4], gas-pressure monitoring [5], and industry applications [6]. Piezo-resistivity-based pressure sensors making use of physic-electronic transduction are the most common sensor type because of their easy signal read-out capability. Many micronanostructures, such as ultrathin gold nanowires [7] and urchin-like hollow carbon spheres [8], were proposed to enhance transduction efficiency. However, electronical sensors still suffer electromagnetic interference, a narrow working temperature range, a small pressure measurement range, and large temperature cross-sensitivity, which make them unusable in a harsh environment. For example, pressure sensing at a high-temperature compressor can play an important role in aeroengine investigation and its active control [9–11]. The compressor exit temperatures are on the order of ~700°C, which prevents the use of traditional electronical sensors without a complex cooling method. In addition, temperature interference is a nerve-wracking obstruction for sensor

performance, since the large and unstable temperature cross-sensitive characteristics of the sensor will deteriorate the measurement even if the sensor survives at high temperatures.

In recent years, fiber-optic pressure sensors fabricated by employing the microelectromechanical systems (MEMS) technology [12–16] have attracted a great deal of attention because of the feasibility of mass production and high consistency. Anodic bonding technology is the usual way to form a sealed vacuum Fabry–Perot (F–P) microcavity between glass and silicon. The pressure sensitivity can be easily adjusted by designing the thickness of elastic silicon diaphragm and the microcavity diameter. Due to the microcavity diameter of MEMS, fiber-optic pressure sensors are not limited to the diameter of the optical fiber [17]; a ~kPa pressure sensitivity can be easily reached. However, in a wide temperature range, temperature cross-sensitivity is inevitably a severe problem. The temperature cross-sensitivity mainly arises for two reasons. One is the residual gas trapped in the microcavity. Although the anodic bonding process is carried out under a high vacuum condition, some gas will be produced and trapped in the microcavity because of the chemical reaction essence of the anodic

bonding process. The residual gas will shrink or expand with temperature change and produce an undesirable force on the inside face of the pressure-sensing diaphragm. The other reason is the thermal stress at the interface between silicon and glass. The thermal stress caused by the thermal expansion mismatch between different materials will cause nonlinear variation of temperature cross-sensitivity. The two factors together lead to worse temperature-related stability and therefore deteriorate the measurement precision. The problem can be relaxed with Au/Au thermal-compression bonding to some degree by reducing gas production and relieving thermal expansion mismatch with an Au film as a buffer layer [14].

Using real-time temperature measurement to compensate for the pressure-temperature cross-error is an alternative method. For example, a hybrid fiber-optic Fabry–Perot interferometer (FPI) fabricated by double-sided anodic bonding of a through-hole-array-structured glass wafer and two silicon wafers for simultaneous pressure and temperature measurement was proposed [15], or temperature information was obtained by fluorescent material glued near the anodic bonding structure [16]. Nevertheless, the degree of temperature compensation effectiveness will depend largely on the temperature stability of the sensor. The compensation may fail in high-precision measurement when the thermal stress has not been eliminated completely. Therefore, reducing temperature cross response is an essential issue to be solved in order to improve pressure measurement accuracy under a wide dynamic temperature range.

In this paper, an all-silicon dual-cavity fiber-optic pressure sensor is proposed and demonstrated. A silicon substrate and a silicon diaphragm with etched cylindrical cavity are bonded together by silicon/silicon direct bonding to form a sealed vacuum F–P cavity for pressure sensing. The vacuum cavity and the silicon substrate act as two microcavities in series connection. We theoretically analyze the effect of thermal stress and residual gas pressure on pressure measurement, which indicates that the low-temperature cross-sensitivity can fundamentally improve the accuracy of pressure measurement over a wide temperature range. The all-silicon structure fabricated with direct bonding solves the problem of interface thermal mismatch, gas building up in the sealed microcavity, and additional reflective coating. The experiment results show that the pressure sensitivity is of ~33.034 nm/kPa under air pressure ranging from 20 to 280 kPa. The pressure-temperature cross-sensitivity of the proposed pressure sensor is as low as ~5.96 Pa/°C, which verifies that the thermal stress and

residual gas issues have been overcome. To our best knowledge, this sensor presents the lowest pressure-temperature cross-sensitivity among the optical fiber pressure sensors with the capability of surviving high temperatures up to 700°C. Moreover, the silicon microcavity can be used for simultaneous temperature sensing, which is also a useful input and can be used for the further temperature compensation process. The optical fiber pressure sensor is promising for a wide range of applications, especially for pressure detection under a wide temperature range.

2. SENSOR CONFIGURATION AND OPERATION PRINCIPLE

Figure 1 depicts the structure and optical interference model of the proposed pressure sensor. The pressure sensor consists of an all-silicon sensing chip, a silica capillary, and a gold-coated single-mode fiber (SMF), which are fixed by high-temperature ceramic adhesive. The all-silicon sensing chip is composed of two silicon layers: the first layer is a thin silicon diaphragm with an etched cylindrical cavity, and the second layer is a thick silicon substrate. The two layers are physically bonded together to form a sealed vacuum cavity. Light propagates through the SMF into the sensing chip and then is partially reflected back at the outer surface (R_1) and the inner surface (R_2) of the silicon substrate and the inner surface of silicon diaphragm (R_3) in turn. The silicon has a high refractive index at 1550 nm, which results in a relatively high reflection. The outer surface of the silicon diaphragm is rough enough so that the light will not be reflected. Thus, additional reflection coating and antireflection coating can be omitted, which increases reliability and temperature stability further by avoiding the possible problem of coating film thermal stress. R_2 and R_3 form a vacuum F–P microcavity, denoted by FP_1. R_1 and R_2 form a silicon F–P microcavity, denoted by FP_2. Also, R_1 and R_3 form a combined long F–P cavity, denoted by FP_3. The three reflected beams will lead to a superposed interference, and the total intensity can be expressed as [18]

$$I_R(\lambda) = I_1 + I_2 + I_3 - 2\sqrt{I_2 I_3}\cos(\phi_1) - 2\sqrt{I_1 I_2}\cos(\phi_2)$$
$$+ 2\sqrt{I_1 I_3}\cos(\phi_1 + \phi_2), \qquad (1)$$

where I_1, I_2, and I_3 are the power intensities of the three reflected beams, and ϕ_1, ϕ_2 are the phase shifts of FP_1 and FP_2, respectively, which are expressed as
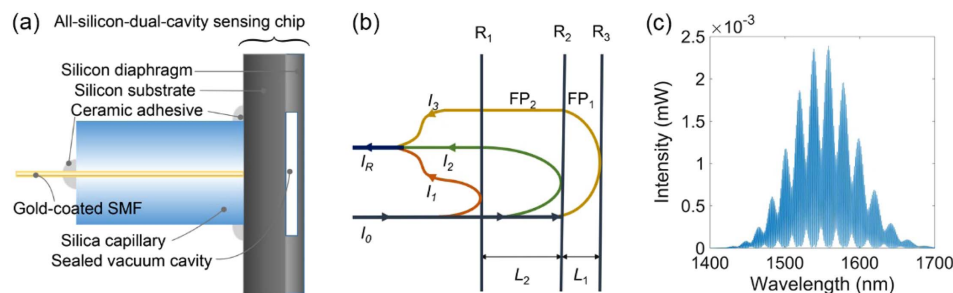

Fig. 1. (a) Schematic diagram of the all-silicon-based dual-cavity fiber-optic pressure sensor structure. (All the components are high-temperature resistant materials.) (b) Interference model of the dual-cavity structure with three reflective mirrors; (c) simulation of reflected spectra $I_R(\lambda)$. (Simulation parameters: $n_1 = 1$, $n_2 = 3.47$, $L_1 = 60$ μm, $L_2 = 300$ μm, I_0 is a broadband light source with a central wavelength of 1550 nm.)

$$\phi_1 = \frac{4\pi n_1 L_1}{\lambda}, \qquad \phi_2 = \frac{4\pi n_2 L_2}{\lambda}, \qquad (2)$$

where n_1 and n_2 are the refractive indices of vacuum and silicon, respectively, and L_1 and L_2 are the cavity length of FP_1 and FP_2. λ is the wavelength of the input light. Equation (1) indicates that the reflection spectrum of the dual-cavity FPI is the sum of three cosine components with different frequencies corresponding to the optical path differences (OPDs) of the three F–P cavities. Each OPD component can be separated and demodulated from the superposition spectra by using Fourier transform combined with the peak-tracing method. With $n_1 \approx 1$, the OPDs of FP_1 and FP_2 are expressed as $OPD_1 = 2L_1$ and $OPD_2 = 2n_2 L_2$. It should be noted that the design of the cavity lengths needs to avoid OPD aliasing.

A. Analysis of Sensing Characteristics of the Vacuum Cavity

As shown in Fig. 2, the cavity length L_1 of FP_1 is sensitive to pressure because the thin silicon diaphragm above the vacuum cavity deforms when external pressure is applied to it. Pressure variation will be transformed into the cavity length variation of FP_1. The deflection of the diaphragm resulting from the longitudinal applied pressure P combined with a lateral load for an edge clamped round diaphragm of uniform thickness can be given by [19]

$$\omega = \frac{3(1 - \nu_1^2)(r^2 - a^2)^2(P - P_R)}{16 E_1 t^3 (1 + \xi)}, \qquad (3)$$

where r is the radius of the cylindrical cavity, a is the radius distance from the SMF center to the cavity center, ν_1 and E_1 are the Poisson's ratio and Young's modulus of silicon, respectively, and t is the effective thickness of the elastic silicon diaphragm. P_R is the residual gas pressure inside the cavity, which can be given as a function of temperature T [20],

$$P_R = \frac{P_{R0} T}{T_0}, \qquad (4)$$

where T_0 is the initial temperature and P_{R0} is the residual gas pressure at T_0. ξ is a compensation factor for the deflection due to a lateral load on the diaphragm, and ξ is given by [19]

$$\xi = \frac{12 \sigma r^2 (1 - \nu_1^2)}{14.68 E_1 t^2}, \qquad (5)$$

where σ is the thermal stress which is related to the properties of the two materials at the bonding interface,

$$\sigma = \frac{(\alpha_1 - \alpha_2) E_1 E_2 (T - T_B)}{(1 + \nu_2) E_1 + (1 - \nu_1) E_2}, \qquad (6)$$
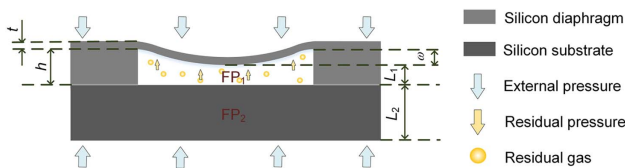

Fig. 2. All-silicon sensing chip's mechanical deformation when external pressure and residual pressure are applied to it. Schematic diagram of the length and thickness of each part of the sensing chip.

where α_1 is the thermal expansion of the diaphragm, α_2, E_2, and ν_2 are the thermal expansion coefficient, Young's modulus and Poisson's ratio of the substrate, respectively, and T_B is the bonding temperature.

In Eq. (3), we define a constant $s_d = 3(1 - \nu_1^2)(r^2 - a^2)^2 / 16 E_1 t^3$ (ignore the dependence of E_1 and ν_1 on temperature), and we will have

$$\omega = \frac{s_d (P - P_R)}{1 + \xi}. \qquad (7)$$

Furthermore, the cavity length L_1 is also related to the original cavity length h. h is affected by the thermal expansion effect of silicon and the strain caused by the lateral pressure. The relationship between them is given by [15]

$$h = h_0 [1 + \alpha_1 (T - T_0)] \left[1 - \frac{1 - 2\nu_1}{E_1} (P - P_0) \right], \qquad (8)$$

where P_0 is the initial atmospheric pressure, T_0 is the initial temperature, and h_0 refers to the initial length of h at T_0 and P_0. Considering all factors, the OPD of FP_1 can be expressed as

$$OPD_1 = 2(h - \omega). \qquad (9)$$

According to Eqs. (3)–(9), the pressure sensitivity S_P of FP_1 can be approximately expressed as

$$S_P = \frac{\partial OPD_1}{\partial P} = -2 \left(\frac{s_d}{1 + \xi} + \frac{1 - 2\nu_1}{E_1} h_0 \right). \qquad (10)$$

The temperature cross-sensitivity S_{Tc} of FP_1 can be approximately expressed as

$$S_{Tc} = \frac{\partial OPD_1}{\partial T}$$
$$= 2 \left[\alpha_1 h_0 + \frac{s_d P_{R0}}{(1 + \xi) T_0} + \frac{s_d \xi (P T_0 - P_{R0} T)}{(1 + \xi)^2 (T - T_B) T_0} \right]. \qquad (11)$$

Thus, the variation of OPD_1 is expressed as $\Delta OPD_1 = S_P \cdot \Delta P + S_{Tc} \cdot \Delta T$. Equations (10) and (11) indicate that both S_P and S_{Tc} are not constant due to the existence of ξ, that is, due to the existence of thermal stress. From Eqs. (5) and (6) we know that if the thermal expansion coefficients of the materials of the diaphragm and substrate are different, the thermal stress will exist and vary with temperature. As a result, with the change of temperature and pressure, variables S_P and S_{Tc} can cause a complicated nonlinear response of FP_1, especially in the case of a large temperature range. The traditional method of using a linear matrix of temperature and pressure can only be used for approximate compensation in a small temperature range, but the compensation effect is not ideal in a wide temperature range. Take the structure fabricated by anodic bonding between silicon diaphragm and pyrex glass substrate as an example: suppose the bonding temperature T_B is 420°C, the residual pressure P_{R0} is 20 kPa, and the structure parameters of the sensor are supposed as we described in the following sensor fabrication section. The OPD response and the pressure measurement errors of FP_1 after compensation are simulated and shown in Fig. 3. It is clear that ΔOPD_1 varies nonlinearly with temperature and pressure in Figs. 3(a) and 3(b). The pressure measurement error increases sharply with a wide range of temperature and pressure changes.
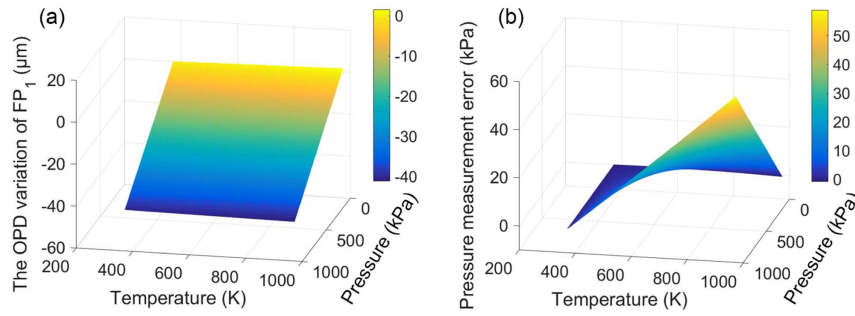
Fig. 3. Simulation results of the nonlinear response characters of the sensor model based on anodic bonding. (a) OPD response of FP_1 with the variation of temperature and pressure; (b) pressure measurement errors of FP_1 by using the traditional linear compensation method.

The maximum measurement error can reach 58.98 kPa when $\Delta P = 1$ MPa and $\Delta T = 600$ K. It can be seen that eliminating thermal stress is the key to improving pressure measurement accuracy.

With our proposed all-silicon structure, there is almost no thermal stress at the bonding interface. Thus, Eqs. (10) and (11) will be simplified to constant values as A and B,

$$S_P = -2\left(s_d + \frac{1 - 2\nu_1}{E_1}h_0\right) = A,$$

$$S_{\text{Tc}} = 2\left(\alpha_1 h_0 + \frac{s_d P_{R0}}{T_0}\right) = B. \tag{12}$$

The pressure-temperature cross-sensitivity of FP_1 is calculated as S_{Tc}/S_P, which is mainly induced by the residual gas pressure P_{R0}. Owing to the silicon direct bonding technique, the gas production is avoided during the bonding process, and hence the residual gas will be reduced. Thus, the all-silicon fiber-optic pressure sensor provides an approach to improving the pressure measurement accuracy from the root of the material and fabrication technique.

B. Temperature Characteristics of the Silicon Cavity

FP_2 can be used for temperature sensing because silicon owns a high thermo-optic coefficient and heat conductivity coefficient. Similarly, the relationship between OPD of FP_2 and the change of pressure and temperature can be written as

$$\text{OPD}_2 = 2L_{20}[1 + \alpha_2(T - T_0)]\left[1 - \frac{1 - 2\nu_2}{E_2}(P - P_0)\right]$$
$$\times [n_{20} + \beta(T - T_0)], \tag{13}$$

where β refers to the thermo-optic coefficient of silicon, and L_{20} and n_{20} refer to the original cavity length and refractive index of silicon at T_0. Actually, over a large temperature range, β is not a constant with temperature [21]. It is approximately linear with temperature as $\beta = \beta_0 + \kappa(T - T_0)$, where β_0 is the thermo-optic coefficient at T_0, and $\kappa = 1.82 \times 10^{-7}$. Ignoring the part $\alpha_2\beta(T - T_0)^2$ in Eq. (13), we have

$$\text{OPD}_2 = 2L_{20}\left[1 - \frac{1 - 2\nu_2}{E_2}(P - P_0)\right][n_{20}$$
$$+ (\beta_0 + \alpha_2 n_{20})(T - T_0) + \kappa(T - T_0)^2]. \tag{14}$$

The pressure cross-sensitivity S_{Pc} of FP_2 can be expressed as

$$S_{\text{Pc}} = \frac{\partial \text{OPD}_2}{\partial P} = -2L_{20}\frac{1 - 2\nu_2}{E_2}[n_{20} + (\beta_0 + \alpha_2 n_{20})(T - T_0)$$
$$+ \kappa(T - T_0)^2]. \tag{15}$$

The maximum of S_{Pc} is calculated to be -7.492×10^{-3} nm/kPa when the temperature changes 700°C. The effect of pressure on OPD_2 is only 7.492 nm under 1 MPa pressure variation (according to the parameters of FP_2 we describe in the following fabrication section), and hence is negligible compared to the temperature sensitivity of FP_2 (111.613 nm/°C). Therefore, Eq. (14) can be simplified as

$$\text{OPD}_2 = 2L_{20}[n_{20} + (\beta_0 + \alpha_2 n_{20})(T - T_0) + \kappa(T - T_0)^2]. \tag{16}$$

The temperature sensitivity S_T can be expressed as

$$S_T = \frac{\partial \text{OPD}_2}{\partial T}$$
$$= 2L_{20}[\beta_0 + \alpha_2 n_{20} + 2\kappa(T - T_0)] = C + 2D(T - T_0), \tag{17}$$

where $C = 2L_{20}(\beta_0 + \alpha_2 n_{20})$, and $D = 2L_{20}\kappa$.

According to Eqs. (12) and (17), the variation of OPDs corresponding to FP_1 and FP_2 can be expressed as a matrix to realize pressure and temperature simultaneous measurement,

$$\begin{bmatrix} \Delta\text{OPD}_1 \\ \Delta\text{OPD}_2 \end{bmatrix} = \begin{bmatrix} A & B \\ 0 & C \end{bmatrix}\begin{bmatrix} \Delta P \\ \Delta T \end{bmatrix} + \begin{bmatrix} 0 \\ D(\Delta T)^2 \end{bmatrix}. \tag{18}$$

It is worth noting that besides passive temperature sensing, the silicon cavity can also be used as an active temperature optical-control medium. 980 nm light can be absorbed by the silicon cavity to heat the sensor [22], which is useful for the sensor under a low-temperature environment to avoid ice formation, or deicing in aviation applications.

3. SENSOR FABRICATION

The all-silicon sensing chip is fabricated by employing MEMS technology. A silicon-on-insulator (SOI) wafer with a device layer of 100 ± 0.5 μm thickness and a double-sided polished silicon wafer with 300 ± 10 μm thickness are chosen as the materials. The size and the orientation of the two wafers are both 100 mm and $\langle 100 \rangle$.
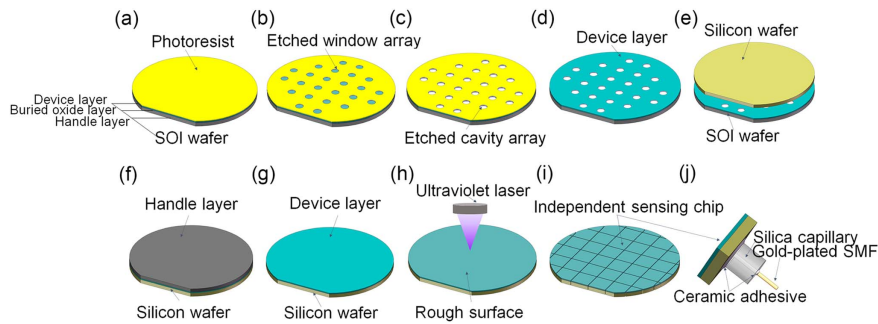
Fig. 4. Fabrication processes of the proposed FPI sensing chip. (a) Spin the photoresist on the surface of the device layer of the SOI wafer; (b) photolithograph with the pre-prepared mask; (c) etch the cavity array by dry etching; (d) remove the photoresist; (e) prebond the SOI wafer with the silicon wafer; (f) anneal the prebonded wafer; (g) remove the handle layer and buried oxide layer by dry etching; (h) roughen the surface of the device layer by ultraviolet laser; (i) dice the bonded wafer into independent sensing chips; (j) assemble the sensing chip with silica capillary and gold-coated SMF.

As shown in Fig. 4, first, we spun the photoresist on the device layer of the SOI wafer [Fig. 4(a)] and used photolithography to make the etching windows with the help of the pre-prepared mask [Fig. 4(b)]. Next, shallow cylindrical cavity arrays with 60-μm depth and 1000-μm radius were fabricated by dry etching so that the device layer with 40-μm thickness was left [Fig. 4(c)]. After removing the photoresist, the SOI wafer and the silicon wafer were cleaned and the surface was activated by wet chemical and plasma treatments to improve the surface hydrophilicity and enhance the bonding properties of the silicon wafers [Fig. 4(d)]. Subsequently, the two wafers were put into the bonder and were aligned and contacted for prebonding [Fig. 4(e)]. During the prebonding process, the vacuum degree was set to 10^{-3} Pa, bonding pressure was maintained at 0.2 MPa, and the temperature was maintained at 420°C. The covalent bonds between wafers are formed by van der Waals force during the prebonding process, which makes the wafers contact closely. To further improve the bonding strength, we need to put the wafers into the furnace after prebonding for the annealing process [Fig. 4(f)]. The temperature was increased up to 1100°C and then cooled naturally. Finally, we removed the handle layer and the buried oxide layer of the SOI wafer by dry etching to leave the device layer only [Fig. 4(g)].

After finishing the MEMS fabrication process, the surface of the device layer was roughened by an ultraviolet laser to eliminate parasitic interference [Fig. 4(h)]. The pure physical process avoids the possible thermal stress induced by an antireflection film. Then the wafer was diced into 5 mm × 5 mm independent sensing chips [Fig. 4(i)]. A gold-plated SMF fiber that can withstand temperatures of 700°C was connected to the sensing chip [Fig. 4(j)]. The SMF was aligned to the center of the silicon substrate surface through a silica capillary and then was fixed by using high-temperature ceramic glue. The picture of the complete sensor is shown in Fig. 5(a), and Fig. 5(b) is the sectional view of a sensing chip and the inset is the detail of the F–P cavity under a microscope; Fig. 5(c) is the top view of the whole bonded wafer before being roughened. The silicon diaphragm above the microcavity obviously sinks under atmospheric pressure.

4. RESULTS AND DISCUSSION

A. Sensor Response to the Pressure Variation

The experimental setup for investigating the pressure characteristic of the proposed optical pressure sensor is shown in Fig. 6. Light from a band board light source propagates into the sensor via a circulator and then the reflected signal will be recorded by the optical spectrum analyzer (Yokogawa AQ6370). We put the sensor into an air pressure chamber. Pressure can be precisely adjusted by a high-accuracy controller (Honeywell ADT-222C) with a precision of 0.02 kPa. The pressure chamber was placed in a thermostat (ESPEC SETH-A-040U) with a precision of 0.5°C to control the surrounding temperature.

A representative interference spectrum obtained at 20°C and 100 kPa is shown in Fig. 7(a). The waveform of low frequency
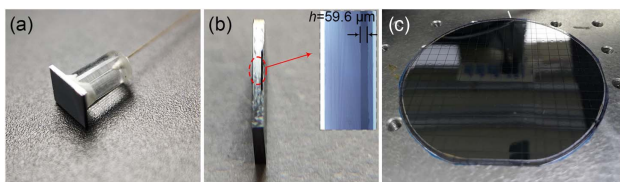

Fig. 5. Pictures of different parts of the fiber-optic pressure sensor structure. (a) Complete sensor after the MEMS process and package; (b) sectional view of a sensing chip and the inset is the detailed section view under a microscope; and (c) top view of the whole wafer before being roughened.
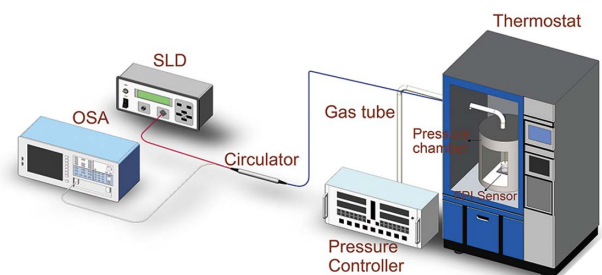

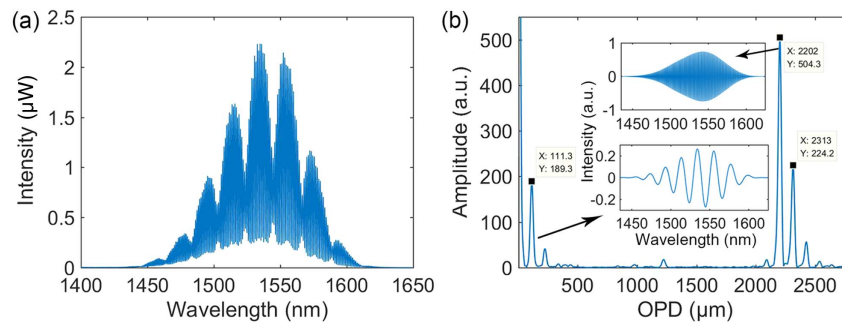**Fig. 6.** Experimental configuration for investigation of the pressure characteristic of the sensor.

Fig. 7. Example of the demodulation process from the reflection spectra. (a) Recorded interference spectra under 20°C and 100 kPa; (b) OPD results after taking fast Fourier transform of the reflection spectra.

is produced by the vacuum cavity FP_1, and the waveform of high frequency is produced by the silicon cavity FP_2 and the combination of the two cavities, FP_3. In order to demodulate the OPDs of the two cavities with large dynamic range and high resolution, the Fourier transform combined with the peak-tracing method is carried out [23]. Figure 7(b) shows the retrieved rough OPDs by taking the fast Fourier transform. The OPDs of 111.3, 2202, and 2313 μm represented by the three distinct peaks correspond to FP_1, FP_2, and FP_3, respectively. The insets in Fig. 7(b) show the extracted independent interference spectra corresponding to FP_1 and FP_2 by using bandpass filters. Combined with the peak-tracing method, the precise OPD measurement results can be obtained.

According to the thin plate or small deflection theory [19], the maximum deformation of silicon diaphragm should be less than 20% of its thickness to ensure that the deformation changes linearly with external pressure. Thus, the maximum measurement pressure is about 385 kPa. The experiment was carried out when the temperature of the thermostat was stabled at –20°C, 0°C, 20°C, 40°C, and 60°C. At each temperature, the pressure was controlled to increase from 20 to 280 kPa, with a step of 20 kPa.

The OPD response of FP_1 and FP_2 at each condition was obtained and is shown in Fig. 8. The relationship between the OPD of FP_1 and pressure is shown in Fig. 8(a). The pressure sensitivity of FP_1, acquired using linear fit, rises slightly from –32.815 nm/kPa to –33.179 nm/kPa, corresponding

to temperature from –20°C to 60°C, which agrees well with the theoretical value $S_P = -32.984$ nm/kPa when $a = 330$ μm. All fitting curves exhibit high linearity ($R^2 = 0.9999$). The slight increase of pressure sensitivity is reasonable due to the decrease of silicon's Young's modulus when the temperature rises. The inset in Fig. 8(a) shows the OPD shift of FP_1 with temperature, with pressure being fixed at 100 kPa. A temperature cross-sensitivity of 0.320 nm/°C is found, which is very close to the theoretical value $S_{Tc} = 0.312$ nm/°C when $P_{R0} = 0$ and $\sigma = 0$. The result indicates that the thermal stress and residual gas both have been greatly reduced compared to the sensor fabricated by the anodic bonding technique [24].

On the other hand, as Fig. 8(b) shows, the OPD of FP_2 remains almost unchanged with pressure increasing to 280 kPa, which demonstrates that the silicon microcavity FP_2 is insensitive to pressure.

B. Sensor Response to the High-Temperature Variation

In order to evaluate the high-temperature performance of the all-silicon pressure sensor, another experimental setup was built, as Fig. 9 shows. We put the sensor directly into a furnace (Lindberg/Blue M BF51866KC-1) to control the surrounding temperature; other instruments remained unchanged.

During the experiment, the sensor was heated up from 100°C to 700°C with a step of 50°C and then was cooled down back to 100°C with the same step. The OPD demodulation
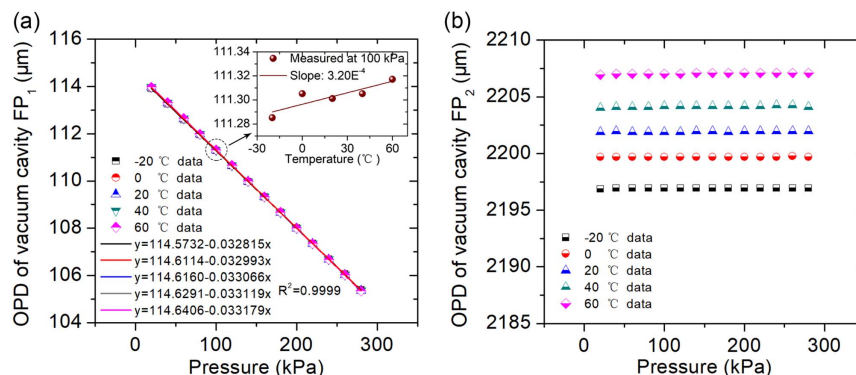

Fig. 8. Demodulation results of OPDs' response to pressure from 20 to 280 kPa at low temperatures. The demodulation results corresponding to (a) vacuum cavity FP_1 and (b) silicon cavity FP_2.
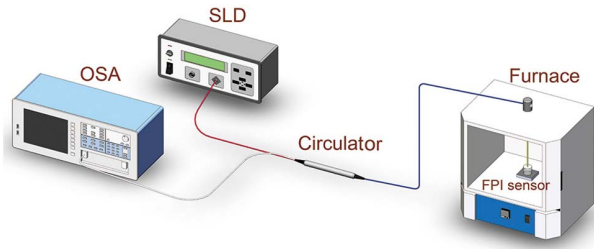
Fig. 9. Experimental configuration for the investigation of the high-temperature characters of the sensor.

results of the high-temperature experiment are shown in Fig. 10.

From Fig. 10(a), it can be observed that OPD of the vacuum cavity FP_1 shifts with temperature linearly with a low-temperature cross-sensitivity of 0.256 nm/°C and 0.261 nm/°C, corresponding to the heating and cooling process, respectively, which is a little smaller than the theoretical value. This is because Young's modulus of silicon decreases with increasing temperature. Since the experiment was carried out over a large temperature range, the silicon diaphragm deformation increased under the same external pressure. On the other hand,

the lower linearity and coincidence in Fig. 10(a) further verified the complication of temperature interference, such as the tiny difference of two silicon wafer materials and tiny gas existence.

In Fig. 10(b), the OPD response of the silicon cavity FP_2 exhibits a quadratic relation with temperature, with no hysteresis. The fittings to the heating and cooling data give the first-order coefficients of 121.670 nm/°C and 124.185 nm/°C, respectively, and the second-order coefficients of 1.05822×10^{-4} nm/(°C)^2 and 1.06166×10^{-4} nm/(°C)^2, respectively, which agree well with the theoretical value of 111.660 nm/°C and 1.09320×10^{-4} nm/(°C)^2.

In summary, from the discussion above, the sensor shows the ultralow temperature cross-sensitivity and excellent stability during the high-temperature cycle experiment. Pressure and temperature can be simultaneously obtained by solving the following matrix equation:

$$\begin{bmatrix} \Delta OPD_1 \\ \Delta OPD_2 \end{bmatrix} = \begin{bmatrix} -33.034 & 0.197 \\ 0 & 122.928 \end{bmatrix} \begin{bmatrix} \Delta P \\ \Delta T \end{bmatrix} + \begin{bmatrix} 0 \\ 0.105994 \times (\Delta T)^2 \end{bmatrix}, \quad (19)$$

where ΔOPD_1 and ΔOPD_2 are in the unit of nanometers, and the units of ΔP and ΔT are in kilopascals and °C, respectively.
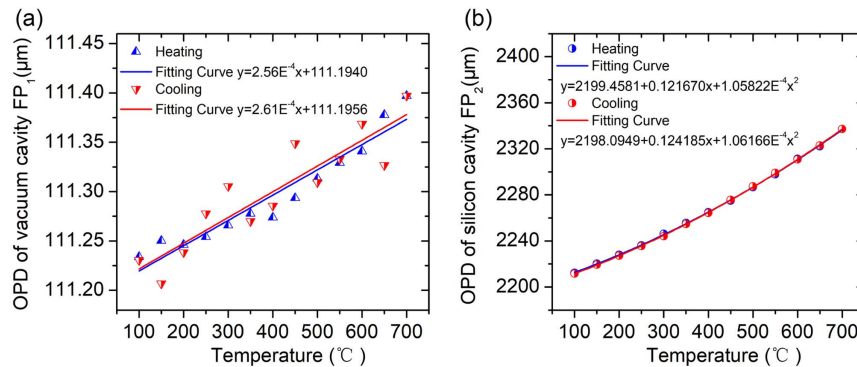

Fig. 10. Demodulation results of OPDs' response to high temperature from 100°C to 700°C under atmosphere environment. The demodulation results corresponding to (a) vacuum cavity FP_1 and (b) silicon cavity FP_2.

Table 1. Comparison of the Proposed Fiber-Optic Pressure Sensors in Terms of Structure, Pressure Sensitivity, Temperature Cross-Sensitivity, and Pressure-Temperature Cross-Sensitivity

Type	Structure	Pressure Sensitivity	Temperature Cross-Sensitivity	Pressure-Temperature Cross-Sensitivity
MEMS	The present work	33.034 nm/kPa	0.197 nm/°C	5.96 Pa/°C
	Silicon-glass-silicon double-sided anodic bonding [15]	12.816 nm/kPa	3.365 nm/°C	263 Pa/°C
	Silicon-glass anodic bonding [16]	~3 nm/kPa	~1.136 nm/°C	~379 Pa/°C
	Silicon-glass thermal compression bonding [14]	47.26 nm/kPa	3.4 nm/°C	71.9 Pa/°C
	All sapphire direct bonding [13]	~5.122 nm/kPa	~2.5 nm/°C	~488 Pa/°C
All-silica	SMF-MMF-silica diaphragm [25]	24.8 nm/kPa	1.48 nm/°C	60 Pa/°C
	SMF-HC-PBF-HCF [26]	1.336 nm/kPa	0.1 nm/°C	74 Pa/°C
	Fiber-tip air bubble FPI [27]	24.44 nm/kPa	2.6 nm/°C	106 Pa/°C
	SMF with side-open F–P cavity [28]	4.071 pm/kPa (wavelength shift)	0.83 pm/°C (wavelength shift)	204 Pa/°C
	SMF fabricated by femtosecond laser [29]	0.56 nm/kPa	8.88×10^{-3} nm/°C	15.86 Pa/°C

The values of *A*, *B*, *C*, and *D* are the average of the experiment data. What is more, as shown in Table 1, compared with the other reported fiber-optic pressure sensors, the pressure sensor proposed in this paper not only has a larger pressure sensitivity but also exhibits an ultralow pressure-temperature cross-sensitivity of ~5.96 Pa/°C. The high-pressure sensitivity and low-pressure temperature cross-sensitivity make the optical pressure sensor attractive for high-temperature pressure measurement applications, such as compressors of aeroengines.

5. CONCLUSION

In this paper, we theoretically analyzed the factors that influence the temperature cross-sensitivity of a microcavity pressure sensor. An all-silicon dual-cavity fiber-optic pressure sensor was successfully fabricated. The sensing chip comprises two silicon layers, which are bonded together by direct bonding. A sealed vacuum F–P microcavity was formed between the silicon substrate and the silicon diaphragm for pressure sensing. The silicon substrate acts as the second solid microcavity for temperature sensing. The sensor can eliminate the influence of thermal stress and residual pressure greatly. The experiment results showed that the ultralow pressure-temperature cross-sensitivity of ~5.96Pa/°C was successfully obtained. In addition, the sensor can survive a temperature of up to 700°C. Therefore, the proposed fiber-optic pressure sensor provides an excellent candidate for pressure measurement in harsh and complicated environments.

Disclosures. The authors declare no conflicts of interest.

REFERENCES

1. S. Sundaram, P. Kellnhofer, Y. Li, J. Zhu, A. Torralba, and W. Matusik, "Learning the signatures of the human grasp using a scalable tactile glove," Nature **569**, 698–702 (2019).
2. C. Wang, D. Hwang, Z. Yu, K. Takei, J. Park, T. Chen, B. Ma, and A. Javey, "User-interactive electronic skin for instantaneous pressure visualization," Nat. Mater. **12**, 899–904 (2013).
3. C. Pang, G. Lee, T. Kim, S. M. Kim, H. N. Kim, S. Ahn, and K. Suh, "A flexible and highly sensitive strain-gauge sensor using reversible interlocking of nanofibers," Nat. Mater. **11**, 795–801 (2012).
4. J. Shin, Y. Yan, W. Bai, Y. Xue, P. Gamble, L. Tian, I. Kandela, C. R. Haney, W. Spees, Y. Lee, M. Choi, J. Ko, H. Ryu, J. Chang, M. Pezhouh, S. Kang, S. M. Won, K. J. Yu, J. Zhao, Y. K. Lee, M. R. MacEwan, S. Song, Y. Huang, W. Z. Ray, and J. A. Rogers, "Bioresorbable pressure sensors protected with thermally grown silicon dioxide for the monitoring of chronic diseases and healing processes," Nat. Biomed. Eng. **3**, 37–46 (2018).
5. F. Yang, F. Gyger, and L. Thévenaz, "Intense Brillouin amplification in gas using hollow-core waveguides," Nat. Photonics **14**, 700–708 (2020).
6. X. Zhou, Q. Yu, and W. Peng, "Fiber-optic Fabry–Perot pressure sensor for down-hole application," Opt. Lasers Eng. **121**, 289–299 (2019).
7. S. Gong, W. Schwalb, Y. Wang, Y. Chen, Y. Tang, J. Si, B. Shirinzadeh, and W. Cheng, "A wearable and highly sensitive pressure sensor with ultrathin gold nanowires," Nat. Commun. **5**, 3132 (2014).
8. L. Shi, Z. Li, M. Chen, Y. Qin, Y. Jiang, and L. Wu, "Quantum effect-based flexible and transparent pressure sensors with ultrahigh sensitivity and sensing density," Nat. Commun. **11**, 3529 (2020).
9. W. J. Pulliam, P. M. Russler, and R. S. Fielder, "High-temperature high-bandwidth fiber optic MEMS pressure-sensor technology for turbine-engine component testing," Proc. SPIE **4578**, 229–238 (2002).
10. W. Ma, Y. Jiang, and H. Gao, "Miniature all-fiber extrinsic Fabry–Pérot interferometric sensor for high-pressure sensing under high-temperature conditions," Meas. Sci. Technol. **30**, 025104 (2019).
11. H. Zhang, J. Liu, J. Li, and P. Jia, "Miniature all-silica microbubble-based fiber optic Fabry-Perot pressure sensor with pressure leading-in tube," J. Sens. **2019**, 5704614 (2019).
12. C. Pang, H. Bae, A. Gupta, K. Bryden, and M. Yu, "MEMS Fabry-Perot sensor interrogated by optical system-on-a-chip for simultaneous pressure and temperature sensing," Opt. Express **21**, 21829–21839 (2013).
13. W. Li, T. Liang, P. Jia, and C. Lei, "Fiber-optic Fabry–Perot pressure sensor based on sapphire direct bonding for high-temperature applications," Appl. Opt. **58**, 1662–1666 (2019).
14. X. Wang, S. Wang, J. Jiang, K. Liu, M. Xiao, X. Chen, D. Zhang, and T. Liu, "An MEMS optical fiber pressure sensor fabricated by Au-Au thermal-compression bonding," Proc. SPIE **10618**, 106180J (2018).
15. J. Yin, T. Liu, J. Jiang, K. Liu, S. Wang, Z. Qin, and S. Zou, "Batch-producible fiber-optic Fabry–Perot sensor for simultaneous pressure and temperature sensing," IEEE Photon. Technol. Lett. **26**, 2070–2073 (2014).
16. X. Jiang, C. Lin, Y. Huang, K. Luo, J. Zhang, Q. Jiang, and C. Zhang, "Hybrid fiber optic sensor, based on the Fabry–Perot interference, assisted with fluorescent material for the simultaneous measurement of temperature and pressure," Sensors **19**, 1097 (2019).
17. J. A. Guggenheim, J. Li, T. J. Allen, R. J. Colchester, S. Noimark, O. Ogunlade, I. P. Parkin, I. Papakonstantinou, A. E. Desjardins, and E. Z. Zhang, "Ultrasensitive plano-concave optical microresonators for ultrasound sensing," Nat. Photonics **11**, 714–719 (2017).
18. Z. Ran, Y. Rao, W. Liu, X. Liao, and K. Chiang, "Laser-micromachined Fabry-Perot optical fiber tip sensor for high-resolution temperature-independent measurement of refractive index," Opt. Express **16**, 2252–2263 (2008).
19. S. P. Timoshenko and S. Woinowsky-Krieger, *Theory of Plates and Shells* (McGraw-Hill, 1959), Chaps. 3 and 12.
20. T. Liu, J. Yin, J. Jiang, K. Liu, S. Wang, and S. Zou, "Differential-pressure-based fiber-optic temperature sensor using Fabry–Perot interferometry," Opt. Lett. **40**, 1049–1052 (2015).
21. F. G. D. Corte, M. E. Montefusco, L. Moretti, I. Rendina, and G. Cocorullo, "Temperature dependence analysis of the thermo-optic effect in silicon by single and double oscillator models," J. Appl. Phys. **88**, 7115–7119 (2000).
22. G. Liu, Q. Sheng, D. Dam, J. Hua, W. Hou, and M. Han, "Self-gauged fiber-optic micro-heater with operation temperature above 1000°C," Opt. Lett. **42**, 1412–1415 (2017).
23. X. Wang, S. Wang, J. Jiang, K. Liu, P. Zhang, W. Wu, and T. Liu, "High-accuracy hybrid fiber-optic Fabry-Pérot sensor based on MEMS for simultaneous gas refractive-index and temperature sensing," Opt. Express **27**, 4204–4215 (2019).
24. X. Wang, S. Wang, J. Jiang, K. Liu, X. Zhang, M. Xiao, H. Xiao, and T. Liu, "Non-destructive residual pressure self-measurement method for the sensing chip of optical Fabry-Perot pressure sensor," Opt. Express **25**, 31937–31947 (2017).
25. X. Guo, J. Zhou, C. Du, and X. Wang, "Highly sensitive miniature all-silica fiber tip Fabry–Perot pressure sensor," IEEE Photon. Technol. Lett. **31**, 689–692 (2019).
26. Z. Zhang, J. He, B. Du, F. Zhang, and Y. Wang, "Measurement of high pressure and high temperature using a dual-cavity Fabry–Perot interferometer created in cascade hollow-core fibers," Opt. Lett. **43**, 6009–6012 (2018).

27. S. Liu, Y. Wang, C. Liao, Y. Wang, J. He, C. Fu, K. Yang, Z. Bai, and F. Zhang, "Nano silica diaphragm in-fiber cavity for gas pressure measurement," Sci. Rep. **7**, 787 (2017).
28. S. Wu, G. Yan, C. Wang, Z. Lian, X. Chen, and S. He, "FBG incorporated side-open Fabry–Perot cavity for simultaneous gas pressure and temperature measurements," J. Lightwave Technol. **34**, 3761–3767 (2016).
29. Y. Zhang, L. Yuan, X. Lan, A. Kaur, and J. Huang, "High-temperature fiber-optic Fabry–Perot interferometric pressure sensor fabricated by femtosecond laser," Opt. Lett. **38**, 4609–4612 (2013).